MAGNETIC BEARING REACTION WHEEL MICRO-VIBRATION SIGNATURE PREDICTION

G. Borque Gallego[1], L. Rossini[1], E. Onillon[1], T. Achtnich[2], C. Zwyssig[2], R. Seiler[3], D. Martins Araujo[4], and Y. Perriard[5]

[1]*CSEM SA, Rue Jaquet-Droz 1, CH-2002 Neuchâtel, Switzerland. Email: guzman.borquegallego@csem.ch, leopoldo.rossini@csem.ch, emmanuel.onillon@csem.ch*
[2]*Celeroton AG, Industriestrasse 22, CH-8604 Volketswil, Switzerland. Email: timon.achtnich@celeroton.com, christof.zwyssig@celeroton.com*
[3]*ESA/ESTEC, Keplerlaan 1, NL-2200 AG Noordwijk, The Netherlands. Email: rene.seiler@esa.int*
[4]*CERN, Esplanade des Particules 1, CH-1211 Geneva, Switzerland. douglas.martins.araujo@cern.ch*
[5]*Integrated Actuators Laboratory, EPFL, Rue de la Maladière 71, CH-2000 Neuchâtel, Switzerland. Email: yves.perriard@epfl.ch*

ABSTRACT

This article presents an analytical micro-vibration model for magnetic bearing reaction wheels (MBRWs) based on a rotordynamics model combined with the active control loop. This model is validated employing a fully-active Lorentz-type MBRW demonstrator and a multi-component dynamometer capable of measuring the exported micro-vibrations. The results show an accurate description of the generated vibration by only considering the unbalance forces as excitation.

Keywords: Magnetic bearing reaction wheel; vibration; modelling.

1. INTRODUCTION

The demand for cost reduction in space missions has led to the development of small spacecraft with more capable payloads, which often implies experiencing a higher sensitivity to mechanical disturbances. In general, the requirement of high pointing accuracy for new telecommunication, Earth observation and scientific telescope missions has tightened the restrictions concerning tolerable levels of on-board disturbances [1], such as micro-vibration generated by different spacecraft actuators, with reaction wheels (RWs) being frequently identified as the most critical sources for small satellites. In order to comply with these requirements, magnetic bearing actuators of compact size and low mass have been identified as a promising solution for small spacecraft.

The main potential advantages of magnetic bearings and the progress in some technological aspects, like the development of rare-earth magnets (i.e. samarium-cobalt magnets), resulted in the first efforts of developing magnetically-suspended reaction wheel systems. These main advantages are, among others, a virtually infinite lifetime, due to friction-less and maintenance-free operation, and better control of bearing dynamic properties. Different magnetic bearing RW topologies, e.g. [2–4], have been presented in the past. They mainly focus on ultra-low disturbance generation, and they usually rely on hybrid topologies, i.e. combining active and passive stabilisation of rotor's degrees of freedom, and focused on rather large spacecraft platforms, such as Aerospatiale's families of MBRWs [5], employed in SPOT 1, 2 or 3 missions among others. These satellites were of approximately 2 tons of weight and needed high restrictions on allowed disturbances.

The growth in importance of small satellites – under $500\,\mathrm{kg}$ of mass – in space missions has led to the study of the applicability of magnetic bearings for these reduced platforms in the recent years [6, 7]. Nevertheless, the challenges involved in the miniaturisation and development of a competitive compact magnetic bearing reaction wheel remain to be solved.

A new and more compact ultra-high-speed magnetic bearing and motor topology has been proposed and developed by the Swiss Federal Institute of Technology in Zurich (ETHZ) and Celeroton AG [8–11], with promis-

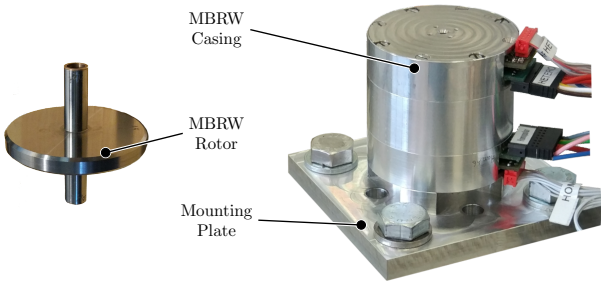

Figure 1. Miniature magnetic bearing reaction wheel demonstrator by Celeroton AG. Rotor with inertia disk (left) and external casing (right).

ing capabilities for space applications, such as reaction wheels for attitude and orbit control systems (AOCS). For studying the capabilities of such a technology for space applications, a magnetic bearing reaction wheel demonstrator has been developed [12,13] that is shown in figure 1.

In order to assess if different reaction wheel systems comply with the allowed mechanical noise requirements in space missions, several on-ground qualification tests are usually performed, like, for instance, at the European Reaction Wheel Characterisation Facility (RCF) [14]. The measured force and torque rely on the combination of different multi-component piezoelectric dynamometric sensor measurements, rigidly mounted, on one side, to an isolation table (big seismic mass over pneumatic isolators), and on the other side, to the test specimen.

Extensive work has already been done for measuring and characterising the micro-vibration type of disturbances generated by conventional ball-bearing reaction wheels (BBRWs) [15, 16], but to the authors knowledge, no similar study has been performed for assessing the noise signature of magnetic bearing reaction wheels. In this article, a characterisation of the main micro-vibration sources for these magnetic actuators is performed, and an analytical model is presented and validated by comparison with experimental micro-vibration data of the aforementioned miniature magnetic bearing reaction wheel demonstrator developed by Celeroton.

2. MICRO-VIBRATION SOURCES

Due to the high impact of reaction wheels on satellite's pointing accuracy, the noise signature and the main sources of these disturbances for common BBRWs have been extensively addressed in the past [15,16]. These disturbances are commonly known as micro-vibration, due to their low amplitude and periodic components, dependent on rotor's speed, and are common to any rotating machinery.

The main sources of periodic reaction wheel microvibration can be classified, as performed in [15], according to their origin or cause in: unbalance-driven , bearing-driven, and motor-driven disturbances.

2.1. Unbalance-Driven Disturbances

This component of the micro-vibration is caused by uneven distribution of mass in the rotor around its geometrical axis, and it is acknowledged to be the most significant disturbance in reaction wheels. It consists of two types of unbalances: static unbalance, which appears as a periodic force perpendicular to the rotation axis, and dynamic unbalance, measurable as a cross-torque, also perpendicular to the spin axis. Both types can be modelled by considering an additional mass in the rotor, and expressed as follows:

$$\begin{aligned} \mathbf{F_s} &= [F_x, F_y]^\top = m_s r_s \Omega^2 [sin(\Omega t), cos(\Omega t)]^\top, \\ \mathbf{T_d} &= [T_x, T_y]^\top = m_d r_d d_d \Omega^2 [sin(\Omega t), cos(\Omega t)]^\top, \end{aligned} \tag{1}$$

where Ω is the wheel rotation speed, m_s and m_d are the static and dynamic unbalance point-masses, respectively, r_s and r_d the radius between the geometric axis of rotation and the static and dynamic masses, and d_d the axial distance between the dynamic unbalance masses. These unbalance models consider a centrifugal force and torque in radial direction (F_x, F_y, T_x, T_y), synchronous with rotation speed. Due to the interaction with other bodies of the reaction wheel assembly (RWA), such as the stator, other modulations of these unbalance can be measured, appearing as higher integer harmonic orders of the rotation frequency.

One of the main advantages of magnetic bearings, due to the lack of physical contact between rotor and stator, is the possibility of including active unbalance control, that would considerably reduce the exported vibrations of the reaction wheel.

2.2. Bearing-Driven Disturbances

For conventional ball bearing RWs, other non-integer modulations of the harmonic micro-vibrations appear as a result of imperfections in the bearing components, originated from the manufacturing process, such as waviness or geometrical irregularities in the surface of bearing parts. Ball bearings also generate random/transient disturbances, mainly due to lubrication issues, such as performance deterioration at close speeds close to zero, limited number of zero-crossings, momentary non-homogeneous oil distribution inside the bearings that generate additional friction force or other disturbances originated from ageing lubricant.

All these disturbances will not appear in a magnetically levitated RW, due to the contactless, and thus, frictionless operation of these actuators. In practice, some permanent magnet and winding imperfections, power electronics and sensors will generate some parasitic forces to the rotor and stator, appearing as integer or non-integer harmonic orders of the rotation frequency. The characteristics of such forces will greatly depend on the magnetic bearing topology and control approach employed, as happens for the motor-driven disturbances.

2.3. Motor-Driven Disturbances

Torque ripple and torque instabilities are the main components of motor-dependent disturbances that appear about rotation axis as a distorting motor torque (M_z). The former is understood as any periodic/deterministic torque disturbance derived from power electronics switching, variation in airgaps between permanent magnets, current measurement errors and cogging torque [16]. The latter is referred to as any random or transient disturbance on the motor torque, such as random torque noise.

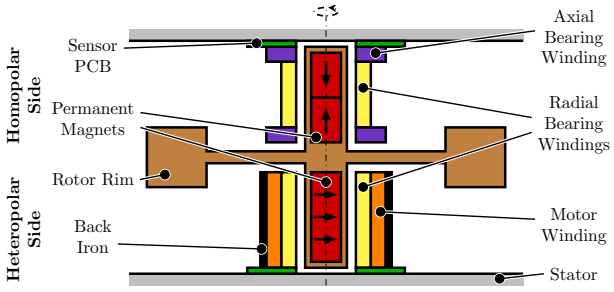

Figure 2. Schematic cross-sectional view of the magnetic bearing reaction wheel demonstrator topology.

3. MINIATURE MAGNETIC BEARING REACTION WHEEL DEMONSTRATOR FOR SMALL SATELLITES

In this section, the miniature magnetic bearing topology will be shown [13]. As mentioned before, the actuator is a Lorentz-type AMB, i.e. all the 6 degrees of freedom (DoF) of the rotor are actively controlled and the force generation is based on electrodynamic principle (Lorentz force).

3.1. Magnetic Bearing and Motor Topology

As shown in Fig. 2, the system is composed of two main parts for bearing and motor – heteropolar and homopolar sides – located at the two axial extremes of the rotor, and provided with an inertial disk that increases its momentum storage and exchange capacity.

On the one hand, the heteropolar side is responsible for generating radial forces and motor torque to the rotor, by means of the interaction between the magnetic flux created by a diametrically-magnetised permanent magnet (PM) and the current applied to a three-phased skewed bearing winding with two pole-pairs, for the force generation, and with a three-phased skewed motor winding with a single pole-pair for torque generation. The heteropolar configuration of this part of the machine requires a synchronous modulation of both motor and bearing currents with rotor's orientation, typical in any field-oriented control of PMSMs. The magnetic circuit is shared by both, motor and bearing actuators (self-bearing), and is closed by a stator core, where the bearing and motor windings are located in the machine's air-gap (slotless design).

On the other hand, the homopolar side has no stator core, and is responsible for generating axial and radial forces. These forces result from the Lorentz force between the magnetic field created by two axially magnetised permanent magnets pointing towards each other and two separated ring-wound coils for the axial forces, and with a radial bearing winding which is essentially the same as the heteropolar's radial bearing winding. As before, a combined magnetic circuit is shared between axial and radial bearings. Nevertheless, the homopolar configuration is independent from rotor's orientation, and thus, actuation control loop is simplified, as no field-oriented control is required.

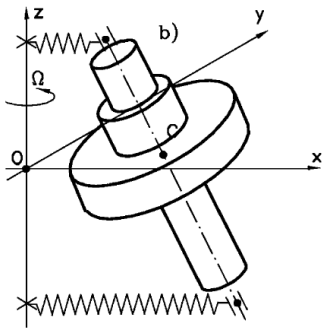

Figure 3. Rigid rotor on compliant bearings and associated reference frame for rotordynamics model (Source: [18]).

The information regarding rotor position and orientation is obtained via two printed-circuit-board (PCB)-based sensors placed at the two axial extremes of the stator. Radial position measurements are based on eddy-current sensors, and axial and angular positions on Hall-effect stray-field measurements [17].

4. ANALYTICAL MICRO-VIBRATION MODEL

In order to predict the generated vibrations during operation, an analytical model is presented, that combines the dynamics of the rotating system and the control loop required for magnetically levitate the rotor. In order to study the generated vibrations in radial directions, the 4 degrees-of-freedom model of radial dynamics presented in [18] or [11] is used. This model is employed not only for estimating the level of micro-vibrations generated by the magnetic bearing reaction wheel, but also to study the general behaviour and stability of the system under different conditions.

As shown in expression (1), the unbalance forces are exclusively radial, and if we consider small radial displacements which holds for this rotordynamics study, the axial dynamics is completely decoupled from the radial one. However, in practice, measurements have shown that the maximum axial forces are at least two orders of magnitude lower than the radial ones, which confirms the previous assumption, and thus axial dynamics are not considered in the following models.

The coordinates of the rigid body are illustrated in figure 3, whose movement while rotating about axis z at speed Ω can be fully characterised by the radial position of its geometrical centre (x_c, y_c) and the radial tilting of the main axes of inertia (ϕ_x, ϕ_y) about axes x and y, respectively.

4.1. Plant Model

Considering the generalised coordinate vector $\boldsymbol{q} = [x_c, \phi_y, y_c, -\phi_x]^\top$, the equations of motion of an un-

damped rigid rotor magnetically levitated and subject to rotor unbalance can be expressed in matrix form as follows

$$M\ddot{\boldsymbol{q}} + G(\Omega)\dot{\boldsymbol{q}} + S\boldsymbol{q} = \boldsymbol{f}_b + \boldsymbol{f}_{ub}(\Omega), \tag{2}$$

being Ω the rotation speed of the rotor, $\boldsymbol{f}_b$ the magnetic bearing forces applied by the actuator's currents, and $\boldsymbol{f}_{ub}$ the unbalance forces. The matrices appearing in the expression are: M, the mass matrix, $G(\Omega)$ the gyroscopic matrix, and S the stiffness matrix. These matrices have the following form:

$$M = diag(m, J_{xy}, m, J_{xy});$$
$$G(\Omega) = \Omega \begin{bmatrix} 0 & 0 & 0 & 0 \\ 0 & 0 & 0 & -J_z \\ 0 & 0 & 0 & 0 \\ 0 & J_z & 0 & 0 \end{bmatrix};$$
$$S = \begin{bmatrix} S_{11} & S_{12} & 0 & 0 \\ S_{12} & S_{22} & 0 & 0 \\ 0 & 0 & S_{11} & S_{12} \\ 0 & 0 & S_{12} & S_{22} \end{bmatrix};$$

where m represents the rotor mass, J_{xy} and J_z the transverse and polar inertia of the rotor, respectively. The subindeces 11 denote a linear-to-linear property, e.g. force in X and displacement in X direction, 12 denote a linear-to-angular property, e.g. torque about X and displacement in Y direction, and 22 denote a angular-to-angular property, e.g. torque about X and tilting in X direction.

The generalised bearing forces $\boldsymbol{f}_b$ are applied to the rotor by means of the electromagnetic force controlled via the input currents $\boldsymbol{u} = [i_{d,1}, i_{q,1}, i_{d,2}, i_{q,2}]^\top$ to the magnetic bearings. The three-phase currents of the radial bearing windings are expressed here in a field-oriented manner, by employing a dq-transformation, as commonly done for rotational machinery [9]. Considering the ideal actuators, these forces can be modelled as follows

$$\begin{aligned} \boldsymbol{f}_b = & \begin{bmatrix} 1 & 0 & 1 & 0 \\ l_{b1} & 0 & -l_{b2} & 0 \\ 0 & 1 & 0 & 1 \\ 0 & l_{b1} & 0 & -l_{b2} \end{bmatrix} \cdot \\ & \cdot diag(\chi_{b1}, \chi_{b1}, \chi_{b2}, \chi_{b2})\boldsymbol{u} = \\ & = V\boldsymbol{u}, \end{aligned} \tag{3}$$

being l_{b1} and l_{b2} the axial distance between the bearing planes and the centre of mass, and χ_{b1} and χ_{b2} the force constants of each magnetic bearing. In practice, the relation between currents and forces can result in a nonlinear expression including cross-couplings between axes, but for the studied Lorentz-type the nonlinearities are small, as it will be shown in the experimental data.

The generalised unbalance forces $\boldsymbol{f}_{ub}$ that are applied to the rotor are originated by the residual unbalance, whose magnitude is characterised by ϵ, the eccentricity of the centre of mass with respect to the geometrical centre of the rotor, and χ the tilting of the main axis of inertia w.r.t. the symmetry axis, resulting in the following structure

$$\boldsymbol{f}_{ub}(\Omega) = \Omega^2 \begin{bmatrix} m\epsilon\cos(\Omega t + \alpha) \\ \chi(J_{xy} - J_z)\cos(\Omega t + \beta) \\ m\epsilon\sin(\Omega t + \alpha) \\ \chi(J_{xy} - J_z)\sin(\Omega t + \beta) \end{bmatrix}. \tag{4}$$

Note that expressions (1) and (4) are equivalent and the unbalance expressed in one form can be easily converted to the other. In order to include such information on the model, the residual unbalance of the rotor can be measured employing a balancing machine, which generally will provide it in terms of $m_s r_s$ and $m_d r_d$ of (1). Then, considering the rotor total mass m, inertia, (J_{xy}, J_z), and the distance between balancing planes d_d, it can be transformed into (4) for the rotordynamics analysis:

$$\epsilon = \frac{m_s r_s}{m}; \quad \chi = \frac{m_d r_d d_d}{J_{xy} - J_z}.$$

Finally, the displacement sensors are located at the two axial extremes of the rotor l_{s1} and l_{s2}. Its measurements $\boldsymbol{y}_{sens}$ can be related to the generalised coordinates, considering small displacements and angles, with the following linear form

$$\boldsymbol{y}_{sens} = \begin{bmatrix} x_{s1} \\ y_{s1} \\ x_{s2} \\ y_{s2} \end{bmatrix} = \begin{bmatrix} 1 & l_{s1} & 0 & 0 \\ 0 & 0 & 1 & l_{s1} \\ 1 & -l_{s2} & 0 & 0 \\ 0 & 0 & 1 & -l_{s2} \end{bmatrix} \boldsymbol{q}. \tag{5}$$

4.2. Controller

The controller architecture is based on a linear-quadratic-gaussian (LQG) observer and controller, and its detailed design is presented in [11].

As shown in figure 4, the control loop for the aforementioned multi-input-multi-output (MIMO) is composed of a controller gain K, a Kalman filter state-space observer, a current limiter and its associated anti-windup for the integral state, and a gravity compensator. At high speeds ($>60\,000\,\mathrm{rpm}$), a generalised notch filter is enabled to reject exported forces due to rotor unbalance, but due to the lower speeds targeted for a RW application, it is omitted here.

The feed-forward component of the currents $\boldsymbol{u}_{ff}$ is computed by considering the gravity magnitude and direction $\boldsymbol{g}$ and injecting directly the current required to apply such a force by means of the inverse matrix V^{-1}.

In order to extract the state vector from the noisy sensor measurements, a Kalman filter of the form

$$\begin{aligned} \begin{bmatrix} \hat{\boldsymbol{q}}(k|k) \\ \hat{\dot{\boldsymbol{q}}}(k|k) \end{bmatrix} = & N_k \begin{bmatrix} \hat{\boldsymbol{q}}(k-1|k-1) \\ \hat{\dot{\boldsymbol{q}}}(k-1|k-1) \end{bmatrix} + \\ & + O_k[\boldsymbol{u}(k-1) - \boldsymbol{u}_{ff}(k-1)] + \\ & + M_k \boldsymbol{y}_m(k), \end{aligned} \tag{6}$$

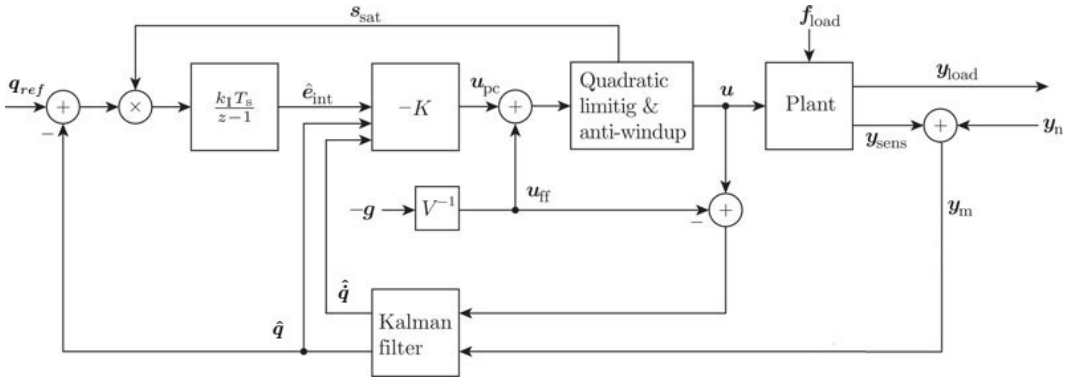

Figure 4. Control scheme of the magnetic bearing reaction wheel demonstrator by Celeroton (Source: [11]).

is used. The estimated state $[\hat{\boldsymbol{q}}, \hat{\dot{\boldsymbol{q}}}]^\top$ at time k is updated by using the estimated state at the previous sample time $k-1$, controller output without gravitational component $(\boldsymbol{u} - \boldsymbol{u}_{ff})$ and sensor measurements $\boldsymbol{y}_m$, multiplied by the observer gain matrices M_k, N_k and O_k.

Considering a reference position $\boldsymbol{q}_{ref} = 0$, to fix the rotor at the geometrical centre of the airgap, the full state feedback LQG controller

$$\boldsymbol{u}_{pc}(k) = -K \begin{bmatrix} \hat{\boldsymbol{e}}_{int}(k|k) \\ \hat{\boldsymbol{q}}(k|k) \\ \hat{\dot{\boldsymbol{q}}}(k|k) \end{bmatrix} \tag{7}$$

is employed. The controller matrix gain K is obtained by minimising a quadratic cost function dependent on states and currents, as typically done for LQG control.

In order to limit the overheating in the bearings, the maximum Joule losses in windings are fixed by imposing a quadratic limit to the input currents $\boldsymbol{u}$. Whenever the threshold is reached the current is limited and integration is stopped via s_{sat}.

4.3. Simulation Environment

The previous plant and controller dynamic equations are combined in a simulation model implemented using MATLAB. This simulation environment is capable of performing the controller design and analyse the closed-loop behaviour of the system. Two types of studies are available:

1. Frequency-based analysis: study of the closed-loop stability and performance in the frequency domain, representative for the steady-state behaviour of the linear/linearised system [8].
2. Time-based analysis: study of the closed-loop behaviour in the time domain, capable of assessing the stability and performance of the system including non-linearities and transient responses.

The latter is the analysis type employed for the micro-vibration simulations due mainly to the possibility of including non-ideal characteristics of the system such as actuator's saturation or non-linearities of the bearings. Furthermore, the same analysis tools employed for the experimental data can be used in order to obtain a more equitable comparison.

In order to do that, the continuous-time equations of motion shown in (2) are considered to describe the dynamics of the system, and the connections of the control loop are performed as shown in figure 4. The evolution of the closed-loop system between each sampling time is then obtained by numerically integrating the dynamics using the fourth-order Runge-Kutta (RK4) method. This way all magnitudes and variables, such as rotor displacements, bearing currents and exported forces, are obtained in the time domain and analysis tools similar to the ones explained in [15] are implemented to obtain the frequency decomposition of the variables for each speed.

In order to analyse the test results, a waterfall plot, i.e. force/torque FFT amplitude vs. speed vs. frequency, allows identifying the noise signature of the wheel. Then, to facilitate the viewing and comparison, a Worst-Case Plot is employed, where the maximum amplitude at every frequency for all the measured speeds is chosen, i.e. maximum force amplitude vs. frequency, allowing the identification of the maximum force or torque for all the range of studied frequencies.

5. EXPERIMENTAL VALIDATION

In order to validate the vibration estimation generated by the proposed analytical method, the following comparison is proposed: the forces measured by an external state-of-the-art multi-component dynamometric platform, F_D, shown in figure 5, and the simulation estimations using the previously defined analytical model, F_S, are compared. This measurement validation set-up has been selected because this type is extensively used for space qualification of equipment in terms of micro-vibration charaterisation. The validation is performed by running the wheel for its whole speed range (from $0\,\text{rpm}$ to $30\,000\,\text{rpm}$) in steps of $1000\,\text{rpm}$, measuring the forces using the dynamometric platform and bearing currents, and simulating the same procedure in the previ-

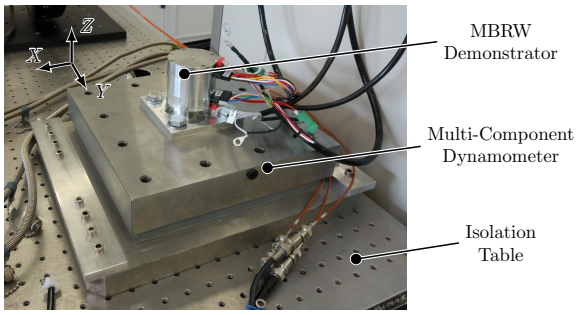

Figure 5. Validation test set-up consisting of the MBRW demonstrator fixed to a Kistler 9255A mounted over an isolation table with its associated X, Y and Z directions.

ously presented simulation model.

An experimental modal testing to identify the combined dynamics of the demonstrator and the test bench has been performed, represented in a transfer function matrix (TFM) $H(\omega)$. This TFM allows to relate the forces in the frequency domain generated by the demonstrator estimated in simulation, $F_S(\omega)$, and the forces measured by the dynamometric platform, $F_D(\omega)$, in order to perform the comparison with its measurements. It is worth mentioning that, as it will be shown in the experimental measurements, an unexpected resonance at $400\,\mathrm{Hz}$ in Y direction was measured, independent of the tested specimen. Even though, the real exported micro-vibrations cannot be measured with this equipment, as the test equipment itself heavily influences the measured forces, it can be used to validate the proposed analytical model combined with the experimental TFM $H(\omega)$.

Firstly, the measurements and simulations in the time domain measured at constant speed for the whole speed range are transformed into the frequency domain via a FFT. The resulting force/torque amplitude vs frequency vs rotor speed is arranged in the form of a Waterfall plot, as shown in figure 6 for the multi-component dynamometer measurements. Secondly, the simulation data is multiplied by TFM $H(\omega)$ for each frequency ω to obtain the simulated exported forces $H(\omega)F_S(\omega)$. Then, the maximum peak for all speeds at each frequency is taken to form a worst-case plot, allowing to directly compare the measured and simulated force and torque amplitudes.

The results of the performed comparison between the exported forces measured by the multi-component dynamometer, $F_D(\omega)$, and the simulated forces filtered by the structure dynamics TFM, $H(\omega)F_S(\omega)$, is shown in figure 7. It can be seen that the simulations are able to correctly extract the main components and characteristics of the measured micro-vibration level and show and accurate estimation of the exported forces and torques, while slightly underestimating the amplitude of the forces and torques.

Vibrations at frequencies higher than $500\,\mathrm{Hz}$ correspond to higher order harmonics of the rotation speed, which are not considered in the model. Nevertheless, specially for torques, these vibrations at higher frequencies are greatly amplified by the structure of the test bench and, in practice, much lower amplitudes are expected.

6. CONCLUSION

The proposed analytical micro-vibration model for a magnetic bearing reaction wheel has been proposed and validated by comparing its simulations to the measurements of a multi-component dynamometer. The results show that, with the only consideration of unbalance in the model, the simulated level of micro-vibrations accurately matches the real vibration level. This implies that for a magnetically-levitated RW, the main source of vibrations is the unbalance of the rotor.

In the future, considering this validated micro-vibration model, an appropriate unbalance control technique will be implemented, which will profit from the magnetic bearing opportunities for the whole speed range and show the capabilities of such a technology. The micro-vibration levels reported in this article are obtained with no vibration suppression algorithm, and thus, an important improvement can be expected.

ACKNOWLEDGMENTS

The authors would like to thank the Swiss Space Center (SSC) and the European Space Research and Technology Centre (ESA/ESTEC) for the technical advice and the possibility of employing their facilities for the validation process, their support and funding under ESA Contract No. 4000108465/13/NL/PA. Furthermore, this activity has been performed in the frame of a Networking/Partnering Initiative (NPI) project involving the Swiss Center for Electronics and Microtechnology (CSEM), the company Celeroton AG, and the European Research and Technology Centre (ESA/ESTEC), under ESA Contract No. 4000119286/17/NL/MH/GM, where a study on active reduction of micro-vibration for active magnetic bearings is being undertaken.

REFERENCES

1. "European Space Technology Harmonisation Technical Dossier," IPC-THAG/ESA, Tech. Rep., 2014.
2. P. A. Studer, "A Practical Magnetic Bearing," in *IEEE Transactions on Magnetics*, Los Angeles, CA, United States, 1977, pp. 1155–1157.
3. A. Nakajima, "Research and Development of Magnetic Bearing Flywheels for Attitude Control of Spacecraft," in *1st International Symposium on Magnetic Bearings*, Zurich, Switzerland, 1988, pp. 3–12.
4. B. Gerlach, M. Ehinger, and R. Seiler, "Low Noise Five-Axis Magnetic Bearing Reaction Wheel," in *IFAC Proceedings Volumes*, vol. 39, no. 16, 2006, pp. 572–577.
5. A. Samuel and B. Lechable, "An Overview on AEROSPATIALE Magnetic Bearing Products for

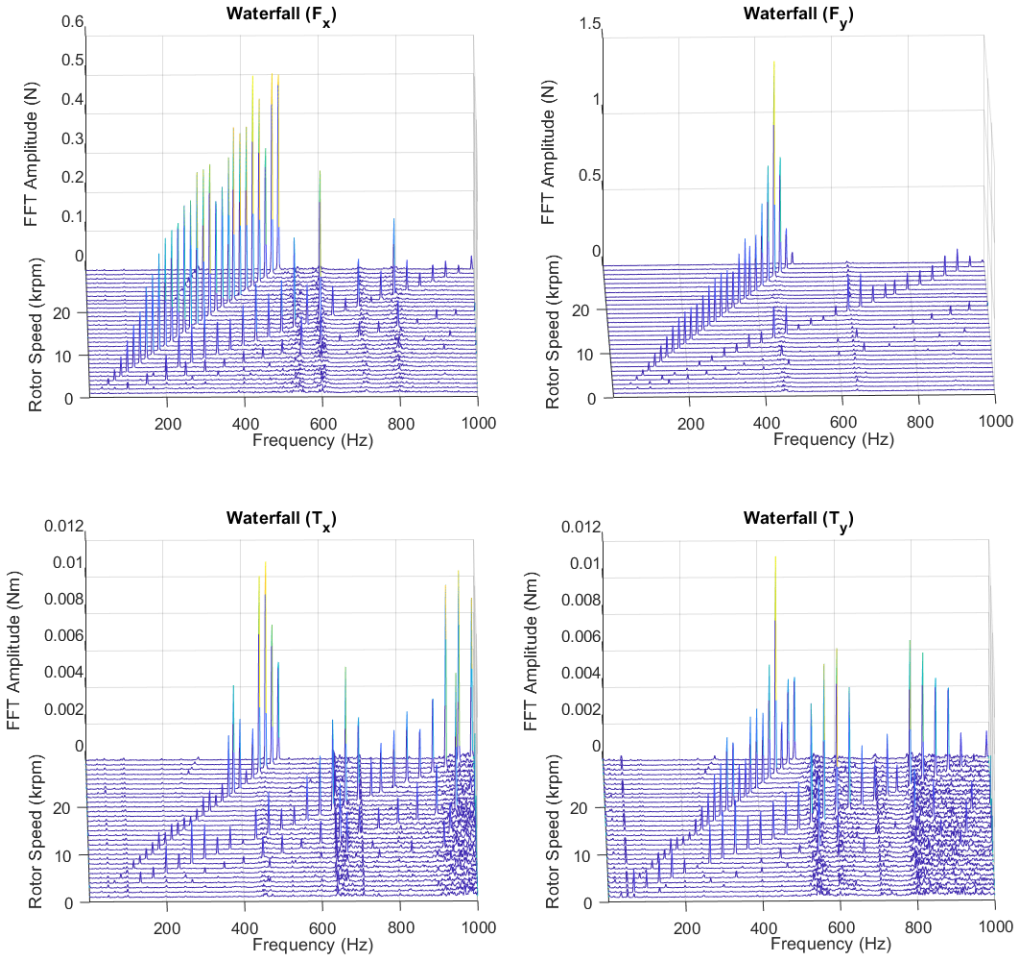

Figure 6. Waterfall plots of micro-vibration level measured by the multi-component dynamometer (F_D) Kistler 9255A at ESA/ESTEC.

Spacecraft Attitude Control and for Industry," in *3rd ESA International Conference Spacecraft Guidance, Navigation & Control Systems*, Noordwijk, the Netherlands, 1996, pp. 217–226.

6. M. Scharfe, T. Roschke, E. Bindl, D. Blonski, and R. Seiler, "The challenges of miniaturisation for a magnetic bearing wheel," in *9th European Space Mechanisms and Tribology Symposium*, vol. 480, Liege, Begium, 2001, pp. 17–24.

7. J. Seddon, "3Dwheel: Attitude Control of Small Satellites Using Magnetically Levitated Momentum Wheels," Ph.D. dissertation, Surrey Space Centre (University of Surrey), 2011.

8. T. I. Baumgartner, "A Magnetically Levitated 500 000 RPM Electrical Drive System," Ph.D. dissertation, ETH Zurich, 2013.

9. A. Looser, T. I. Baumgartner, J. W. Kolar, and C. Zwyssig, "Analysis and Measurement of Three-Dimensional Torque and Forces for Slotless Permanent-Magnet Motors," *IEEE Transactions on Industry Applications*, vol. 48, no. 4, pp. 1258–1266, 2012.

10. T. I. Baumgartner, R. M. Burkart, and J. W. Kolar, "Analysis and Design of a 300-W 500 000-r/min Slotless Self-Bearing Permanent-Magnet Motor," *IEEE Transactions on Industrial Electronics*, vol. 61, no. 8, pp. 4326–4336, 2014.

11. T. I. Baumgartner and J. W. Kolar, "Multivariable State Feedback Control of a 500 000-r/min Self-Bearing Permanent-Magnet Motor," *IEEE/ASME Transactions on Mechatronics*, vol. 20, no. 3, pp. 1149–1159, 2015.

12. C. Zwyssig, T. I. Baumgartner, and J. W. Kolar, "High-Speed Magnetically Levitated Reaction Wheel Demonstrator," in *International Power Electronics Conference - ECCE Asia (IPEC 2014)*, Hiroshima, Japan, 2014, pp. 1707–1714.

13. M. Kaufmann, A. Tüysüz, J. W. Kolar, and C. Zwyssig, "High-Speed Magnetically Levitated Reaction Wheels for Small Satellites," in *23rd International Symposium on Power Electronics, Electrical Drives, Automation and Motion (SPEEDAM 2016)*, Anacapri, Capri, Italy, 2016, pp. 28–33.

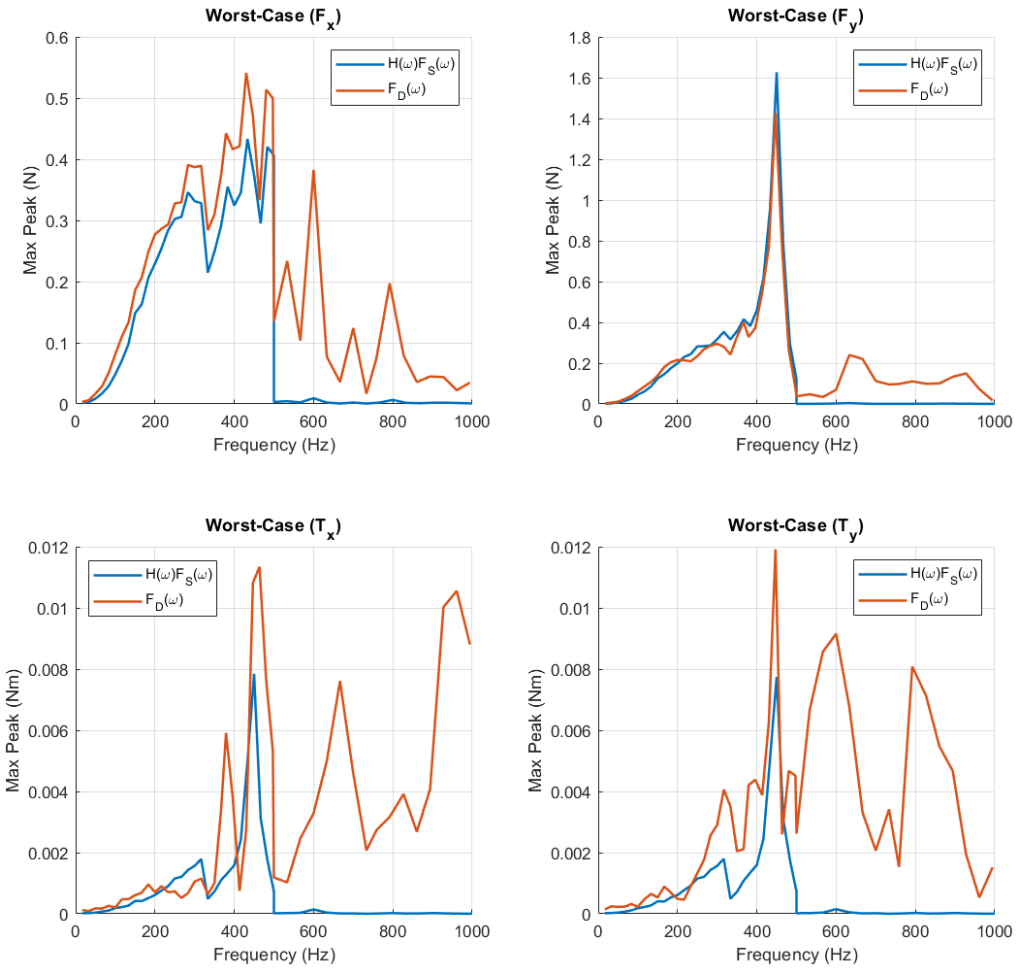

Figure 7. Comparison of worst-case plots between the measurements of multi-component dynamometer (F_D) Kistler 9255A and analytical simulation ($H(\omega)F_S$).

14. M. Wagner, S. Airey, G. Piret, and M. P. Le, "European Space Agency (ESA) New Reaction Wheel Characterisation Test Facility (RCF)," in *35th AAS Guidance and Control Conference*, Breckenridge, Colorado, 2012.

15. H. Heimel, "Spacewheel Microvibration: Sources, Appearance, Countermeasures," in *8th International ESA Conference on Guidance, Navigation & Control Systems*, Karlovy Vary, Czech Republic, 2011.

16. M. P. Le, "Micro-disturbances in reaction wheels," Ph.D. dissertation, Eindhoven University of Technology, 2017.

17. R. Larsonneur and P. Bühler, "New Radial Sensor for Active Magnetic Bearings," in *9th International Symposium On Magnetic Bearings*. Lexington, KY, USA: University of Kentucky, 2004, pp. 495–499.

18. G. Genta, *Dynamics of Rotating Systems*, ser. Mechanical Engineering Series. New York, NY: Springer US, 2005.